The Astrophysical Journal, 965:77 (9pp), 2024 April 10 https://doi.org/10.3847/1538-4357/ad3218

Morphological Evolution of Disk Galaxies and Their Concentration, Asymmetry, and Clumpiness (CAS) Properties in Simulations across Toomre's Q Parameter

T. Chantavat[1], S. Yuma[2], P. Malelohit[2], and T. Worrakitpoonpon[3]
[1] The Institute for Fundamental Study, Naresuan University, Phitsanulok 65000, Thailand
[2] Department of Physics, Faculty of Science, Mahidol University, Bangkok 10400, Thailand
[3] Institute of Science, Suranaree University of Technology, Nakhon Ratchasima 30000, Thailand; worraki@gmail.com
Received 2024 January 12; revised 2024 March 4; accepted 2024 March 7; published 2024 April 9

Abstract

We investigate the morphological and structural evolution of disk galaxies in simulations for a wide range of Toomre's Q parameters. In addition to the inspection of conventional bar modes, we compute the concentration, asymmetry, and clumpiness (CAS) parameters to enlarge the understanding of the galaxy evolution. These parameters are widely employed to analyze the light distribution of the observed galaxies, but the adaptation to numerical simulations is not much considered. While the bar formation takes place in a considerable range of Q around 1, barred galaxies originating from $Q > 1$ and $Q < 1$ disks yield CAS values that differ significantly. Disks starting with $Q < 1$ develop clumps due to local gravitational instabilities along with the bar, and these clumps play a central role in enhancing the CAS values. This process is absent in the $Q > 1$ counterparts in which the evolution is dominated by linearly unstable two-armed modes that lead to lower CAS values. Likewise, unbarred galaxies that are obtainable from disks with Q far below and far above 1 exhibit greatly different CAS magnitudes. It turns out that the CAS parameters can serve as indicators of the initial kinematical state and the evolution history of a disk of any morphology. In addition, we find an alternative mechanism of the formation of the lopsided barred galaxy when $Q \lesssim 1$. Bars that evolve in the midst of the clumps can spontaneously become lopsided at the end.

Unified Astronomy Thesaurus concepts: Galaxy dynamics (591); Barred spiral galaxies (136); Galaxy formation (595); N-body simulations (1083)

1. Introduction

Disk galaxies constitute an important fraction in the Hubble sequence, and their morphologies manifest great diversities, such as spiral, barred-spiral, and lenticular shapes. However, their origins are not fully understood so far. In the standard theoretical framework, substructures in the disk components are considered as amplified perturbations of various forms. For instance, the galactic bar is the remnant of the preceding linearly unstable two-armed modes (Kalnajs 1971; Contopoulos & Papayannopoulos 1980; Vauterin & Dejonghe 1996; Jalali & Hunter 2005). On the other hand, the spiral structures can be achieved by a spiral density wave (Lin & Shu 1964), a sheared gravitationally unstable medium (Goldreich & Lynden-Bell 1965), or sheared synchronized epicyclic motion (Julian & Toomre 1966; Toomre 1981; De Rijcke et al. 2019).

Despite the well-formulated theoretical frameworks, numerical simulations unveiled much intricacy when it was found that the final disk morphologies depended strongly on the intrinsic properties of the disk and halo. A number of simulations demonstrated that the Toomre Q parameter (Toomre 1964) could determine how a circular disk evolved morphologically (Hohl 1971; Athanassoula & Sellwood 1986; Curir et al. 2006; Bekki 2023; Worrakitpoonpon 2023). Otherwise, it was proved that the random kinetic energy of the disk can be used as an indicator of the fate of a disk (Ostriker & Peebles 1973; Efstathiou et al. 1982; Athanassoula 2008; Romeo et al. 2023). In a larger scope, the concern of the disk stability was not only limited to the initial kinematical disk properties, but the physical and kinematical halo properties were also found to be important to the subsequent disk evolution. Many works reported the correlation between the halo/bulge mass concentration and the stability against bar modes (Sellwood 1980, 2016; Sellwood & Evans 2001; Athanassoula & Misiriotis 2002; Shen & Sellwood 2004; Athanassoula et al. 2005; Sheth et al. 2008; Kataria & Das 2018; Saha & Elmegreen 2018; Kataria & Das 2019; Kataria et al. 2020; Jang & Kim 2023). The halo spin was also found to affect the dynamical disk evolution (Saha & Naab 2013; Long et al. 2014; Collier et al. 2019; Kataria & Shen 2022; Li et al. 2023; Chiba & Kataria 2024; Joshi & Widrow 2024). On the other hand, the formation of the spiral structure rather relied on local effects, such as local instabilities and disk shearing (D'Onghia et al. 2013; Fujii et al. 2018; Michikoshi & Kokubo 2020). The cold disk environment was the favorable condition for the formation of spiral arms (Evans & Read 1998; Zakharova et al. 2023), whereas a thick disk tended to suppress this process (Ghosh & Jog 2018; Bauer & Widrow 2019). Unlike the bar component, the formation and evolution of the spiral structures depended less strongly on the choice of halo parameters (Sellwood 2021).

In the observational aspect, morphological studies of galaxies started from a basic visual classification to the classification via the physical properties of the galaxies. The classic Hubble sequence classified galaxies into elliptical, spiral, and irregular galaxies based on the apparent stellar distribution of galaxies (Hubble 1926). The visual inspection, however, has limitations for distant galaxies, as their surface brightness drops due to the cosmological dimming effect. Features such as spiral arms may become too faint to be detected at high redshift (e.g., Papaderos et al. 2023). In fact, distant star-forming galaxies do not share the same structure or

morphology as the local spiral galaxies (Yuma et al. 2011, 2012). Star-forming galaxies started to show a similar structure as those in the local Universe at $z < 0.85$ (Takeuchi et al. 2015).

Another approach is to fit the azimuthally averaged surface brightness profile with a predesignate formula, such as de Vaucouleurs, exponential, and Sérsic profiles (de Vaucouleurs 1948; Sérsic 1963). This method is efficiently used to distinguish an elliptical from a spiral galaxy in the local Universe (e.g., Fischer et al. 2019; Domínguez Sánchez et al. 2022) up to very high redshifts of $z = 16$ (Ono et al. 2023). However, a bulge-disk decomposition by fitting two components of Sérsic and exponential profiles to the galaxies is sometimes physically unrealistic when the Sérsic index of the bulge is as high as $n \sim 8$ (Fischer et al. 2019).

The nonparametric measurement of the light distribution in a galaxy has been intensively introduced to diminish the effect of the model or assumption (e.g., Bershady et al. 2000; Conselice et al. 2000; Conselice 2003, 2014). The concentration (C), asymmetry (A), and clumpiness (S) indices, or the so-called CAS system, are among the most common nonparametric methods used to study the galaxy structure. In addition to their efficiency in classifying elliptical and spiral galaxies, the CAS parameters are related to the evolution of galaxies (Conselice 2003). The concentration index is correlated with the bulge-to-total ratio and stellar mass of the galaxies, while the clumpiness showed a strong correlation with the Hα equivalent width, which is indicative of the star-forming activity. The CAS system has recently been used to study the galaxy structure and its evolution at high redshifts with data obtained with the James Webb Space Telescope (Kartaltepe et al. 2023). Although various studies have used the CAS parameters in numerical simulations, they mainly focused on the merging process of the galaxies (e.g., Conselice 2006; Lotz et al. 2008, 2010a, 2010b).

In this work, we proceed to investigate the morphological disk evolution starting from various Toomre Q parameters. Apart from the inspection of the conventional bar modes, we enlarge our scope to the CAS properties and determine how they can be relevant to observations. These parameters are widely employed to examine the structural properties of observed galaxies, and we adopt them for an analysis of the numerical simulations in this study. The article is organized as follows. First, Section 2 describes the numerical models and accuracy controls. Next, in Section 3, we introduce the parameters used in this work, including those for probing the global nonaxisymmetric features and the CAS indices. Then, Section 4 reports the numerical results, and discussions are provided therein. Finally, Section 5 concludes this study.

2. Numerical Simulations and Accuracy Controls

The self-gravitating N-body simulations are handled by GADGET-2 (Springel et al. 2001; Springel 2005). The density profile of a disk of particles follows an exponential profile with a vertical distribution that reads

$$\rho_d(r, z) = \frac{M_d}{4\pi R_0^2 z_0} e^{-r/R_0} \operatorname{sech}^2\left(\frac{z}{z_0}\right), \quad (1)$$

where M_d is the disk mass, R_0 is the disk scale radius, and z_0 is the disk scale height. We choose $M_d = 10^9\, M_\odot$, $R_0 = 5$ kpc, and $z_0 = 0.2$ kpc. The disk is radially and vertically truncated at $5R_0$ and $5z_0$, respectively. We principally investigate disks of 5×10^6 particles unless otherwise specified. To properly imitate the disk evolution in a dark matter halo, the disk is placed in a static spherical Hernquist potential given by

$$\Phi_h(r) = -\frac{GM_h}{r + r_h}, \quad (2)$$

where M_h and r_h are the halo mass and the halo scale radius, which are fixed to $2.5 \times 10^{10}\, M_\odot$ and 75 kpc. The radial Q profile corresponds to the ratio of the radial velocity dispersion σ_r to the minimum required value for the local stability according to the Toomre criterion (Toomre 1964), i.e.,

$$Q = \frac{\sigma_r \kappa}{3.36 G \Sigma}, \quad (3)$$

where κ is the epicyclic frequency calculated from the composite disk-halo potential $\Phi_{\rm tot}$. In Equation (3), Σ is the disk radial surface density, which is proportional to e^{-r/R_0}. To construct a disk of particles in dynamical equilibrium with a static halo potential, we adopt the prescriptions of Hernquist (1993) for the disk velocity structures. The squared radial velocity dispersion is proportional to the disk surface density, namely

$$\sigma_r^2 \propto e^{-r/R_0}. \quad (4)$$

The constant of the proportionality in Equation (4) is adjusted so that the Q value calculated by Equation (3) at $2R_0$, i.e., the reference radius, is equal to a chosen Q value, and this Q is the representative Q for a case. In other words, a specific Q can be obtained by properly adjusting the constant of proportionality in Equation (4). The tangential velocity dispersion σ_θ is obtained by the relation

$$\sigma_\theta^2 = \frac{\kappa^2}{4\Omega^2}\sigma_r^2, \quad (5)$$

where Ω is the angular frequency of circular orbit calculated from $\Phi_{\rm tot}$. The vertical velocity dispersion σ_z relates to Σ as

$$\sigma_z^2 = \pi G z_0 \Sigma. \quad (6)$$

By these choices, we have $\sigma_z^2 \propto \sigma_r^2$. The mean tangential velocity $\bar{v}_\theta$ as a function of radius is obtained by the axisymmetric Jeans equation as follows:

$$\bar{v}_\theta^2 = r\frac{d\Phi_{\rm tot}}{dr} + \frac{r}{\Sigma}\frac{d(\sigma_r^2\Sigma)}{dr} + \sigma_r^2 - \sigma_\theta^2, \quad (7)$$

whereas the mean radial and vertical velocities (or $\bar{v}_r$ and $\bar{v}_z$, respectively) are initially zero. The three random velocity components are drawn from the cutoff Gaussian distribution with the corresponding local velocity dispersion ellipsoid.

Calculations of spline-softened mutual forces for disk particles are facilitated by the tree code. We adjust the opening angle to 0.7 and the softening length to 5 pc for all particles. The integration time step is controlled to be no greater than 0.2 Myr. The accuracy is such that the deviations of both the total energy and the disk angular momentum at the end of the simulation, which is specified to be 9.6 Gyr, from the initial values are no greater than 0.1%. We examine the cases where $Q = 0.65$, 0.8, 0.95, 1.1, 1.2, and 1.5.

3. Parameters

3.1. Bar Parameter

The nonaxisymmetric features of a disk can be evaluated by the m-mode Fourier amplitudes as a function of radius $\tilde{A}_m(r)$, defined as

$$\tilde{A}_m(r) = \frac{\sqrt{a_m^2 + b_m^2}}{A_0}, \tag{8}$$

where a_m and b_m are the m-mode Fourier coefficients calculated from particles inside an annulus of radius r, and A_0 is the corresponding $m = 0$ amplitude. The m-mode strength A_m is designated by the maximum $\tilde{A}_m$ within $r_{\max}$, or

$$A_m \equiv \max_{r<r_{\max}} [\tilde{A}_m], \tag{9}$$

where we fix $r_{\max}$ to 10 kpc for all calculations. We employ A_2 as the bar strength.

3.2. CAS Parameters

The CAS system is a nonparametric measurement of the light distribution of a galaxy. In the simulations, we obtain the surface density instead of the surface brightness. So we assume a constant mass-to-light ratio across the entire simulated galaxy to translate the surface density into the surface brightness. It consists of three parameters: concentration (C), asymmetry (A), and clumpiness (S). We adopt the concentration index originally defined by Bershady et al. (2000) as

$$C = 5 \log_{10}\left(\frac{r_{80}}{r_{20}}\right), \tag{10}$$

where r_{20} and r_{80} are the radii governing 20% and 80% of the growth curve within 1.5 times the Petrosian radius at $r(\eta = 0.2)$.

The asymmetry index shows the fraction of the galaxy component that is not symmetric, which was originally defined as

$$A = \min\left(\frac{\sum|I_0 - I_{180}|}{\sum|I_0|}\right) - \min\left(\frac{\sum|B_0 - B_{180}|}{\sum|I_0|}\right), \tag{11}$$

where I_0 and B_0 are the original image and background area close to the galaxy, respectively (Conselice et al. 2000). I_{180} is the image after a rotation of 180° from the center of the galaxy in the line of sight. The center is varied until we obtain the minimum value of the asymmetry index. To reduce the effect of noise, Conselice et al. (2000) consider the background region near the object by randomly selecting its center, rotating the background by 180°, and calculating the rightmost term of Equation (11). However, we do not have noise in the simulation. So we simply use only the first term of Equation (11) to estimate an asymmetry index. That is,

$$A = \min\left(\frac{\sum|I_0 - I_{180}|}{\sum|I_0|}\right). \tag{12}$$

Last, the clumpiness index is defined as the ratio of light in a high-frequency structure to the total light of the galaxy (Conselice 2003). It can be written as

$$S = 10 \times \left[\left(\frac{\sum(I_{xy} - I_{xy}^{\sigma})}{\sum I_{xy}}\right) - \left(\frac{\sum(B_{xy} - B_{xy}^{\sigma})}{\sum I_{xy}}\right)\right], \tag{13}$$

where I_{xy} is the original image, while I_{xy}^{σ} is the smoothed image. Likewise, B_{xy} and B_{xy}^{σ} are the original and blurred backgrounds with an area equal to the size of the galaxy (Conselice 2014). The original image is smoothed with a two-dimensional Gaussian kernel with a size of $\sigma = 0.3 \times r(\eta = 0.2)$ (Conselice 2003).

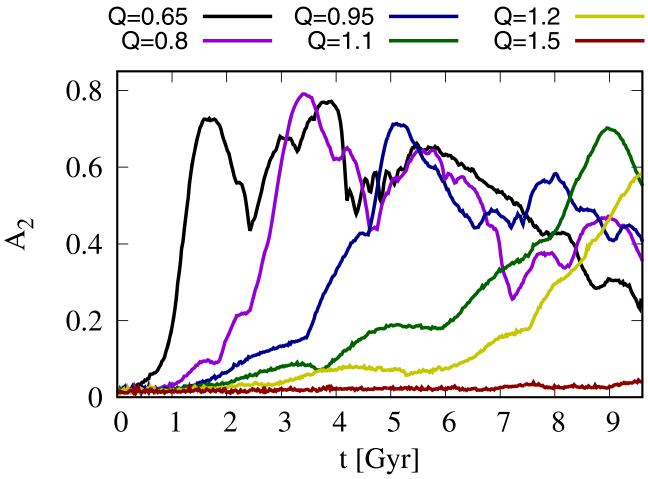

Figure 1. Time evolution of A_2 for disks with different Q.

4. Numerical Results

4.1. Evolution of Bisymmetric Modes

First of all, we inspect the time evolution of A_2 for disks with different Q in Figure 1. It turns out that the development of the bar modes takes place when $Q \leqslant 1.2$. Even though Q is lower than 1, the $m = 2$ modes can still grow in the midst of the local instabilities. A disk with lower Q tends to form a bar more rapidly, in accordance with previous studies (Athanassoula & Sellwood 1986; Hozumi 2022). On the other hand, the value of $Q = 1.5$ is sufficient to suppress the bar instability. We further examine the disk configuration for different Q in Figure 2 to verify the growth of the bar modes. In the case where $Q = 1.1$, we observe the buildup of weak multiarmed modes at 5.52 Gyr, which are overseen by the swing amplification (Julian & Toomre 1966; Toomre 1981). This mechanism engenders the spiral arms from the synchronized epicyclic motion in combination with the disk shearing. After 8 Gyr, the two-armed modes dominate the multiarm modes as the configuration takes the form of the two-armed barred structure, and it remains in this shape until the end. When $Q = 0.95$, which is slightly below the local stability threshold, we observe a more rapid formation of the bar amidst the local instabilities as the bar is spotted at 5.04 Gyr. Compared to the previous case, we remark clumpy subarms around the central bar. As time progresses, the shape of the bar and spiral arms deviates from bisymmetry, and they are surrounded by long-lasting clumps that remain until the end. The clumps emerge from the gravitationally unstable fluctuations, so they are distributed randomly in the disk environment. We speculate that the breaking of the bisymmetry is attributed to those local

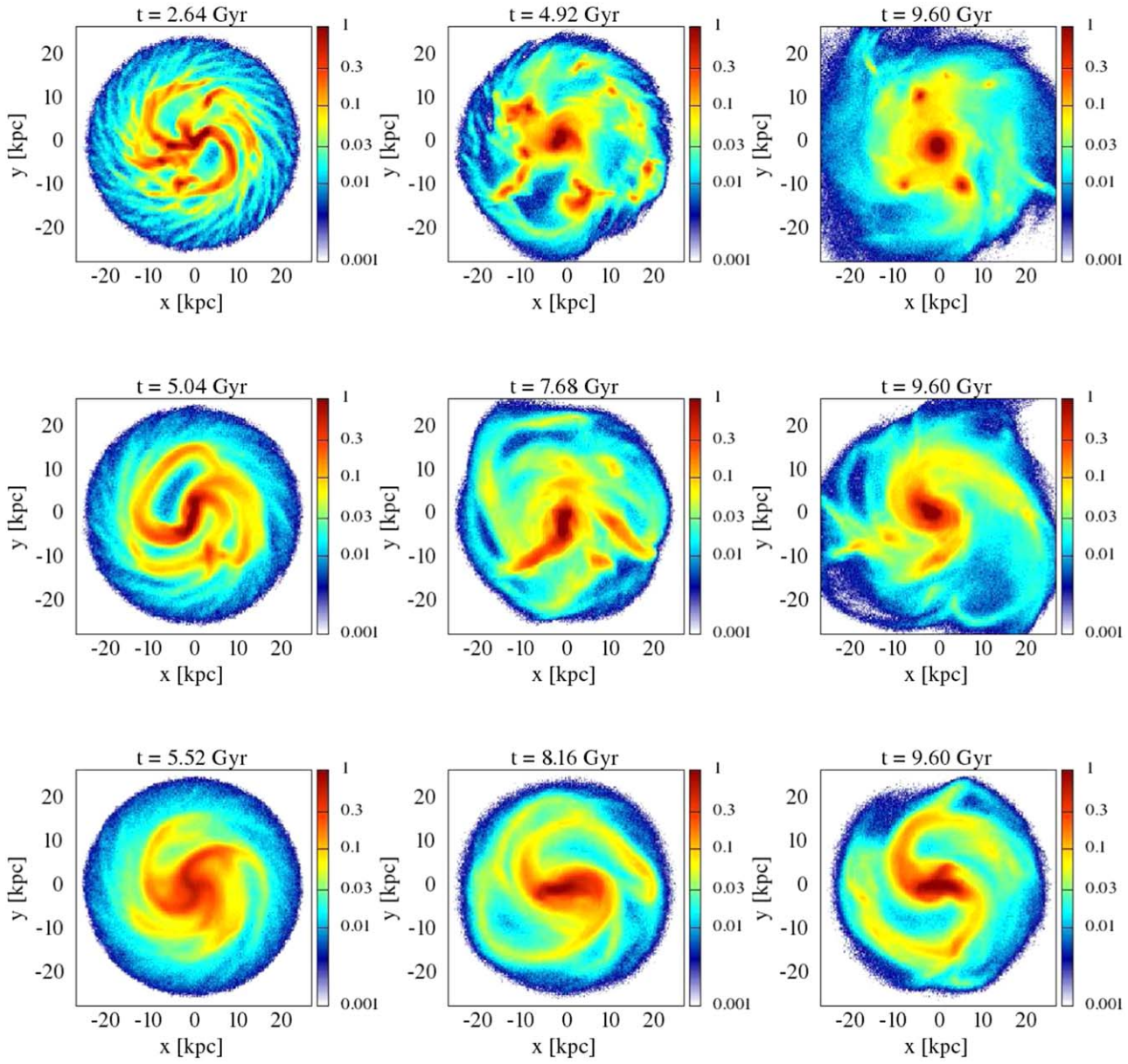

Figure 2. Disk surface density map for $Q = 0.65$ (top row), 0.95 (middle row), and 1.1 (bottom row) at the indicated times.

instabilities and that the bar evolution in the midst of these instabilities can be described as follows. While the two-armed modes are growing, the unstable local over-densities progress to clumps in random places in parallel. Afterward, the bisymmetric component is deformed by the interactions with clumps, as observed in the last snapshot.

The case where $Q = 0.65$ is fully governed by local gravitational instabilities, which leads to a different morphological evolution from the other cases. The mass concentrations develop quickly, supposedly on the timescale of the local freefall time, before they are sheared by the differential disk rotation. As a consequence, the multiarmed spiral pattern is formed rapidly within ∼2.6 Gyr, which is significantly shorter than the timescale of the bar formation. The spiral arms appear to be more clumpy than those arising from the unstable two-armed modes or the swing amplification when $Q > 1$. These arms are short-lived as they are found to be fragmented into clumps at 4.92 Gyr. The clumps are still spotted around the concentrated disk center at the end of the simulation. The fragile spiral structure is another indication that the local instability dominates the spiral mode instability, which plays an important role in other cases. The plot of the density map shows that, referring to Figure 1, the growth of A_2 does not signify the development of the barlike structure. The developed $m = 2$ mode amplitudes are caused by the anisotropically distributed clumps. We note that the number of clumps, in the end, reduces from the number in the snapshot before, which might be due either to the merger between them or to the falling to the disk center. The decrease in the clump number is in accordance with the decline of A_2 with time near the end. In addition, we note that the circular disk symmetry is broken by clumps, which can be explained by the same arguments as for the breaking of the bisymmetry of the barred-spiral structure in the $Q = 0.95$ case.

The bar formation in a disk with $Q \geqslant 1$ conforms with past mainstream studies, but only a few studies visited the regime

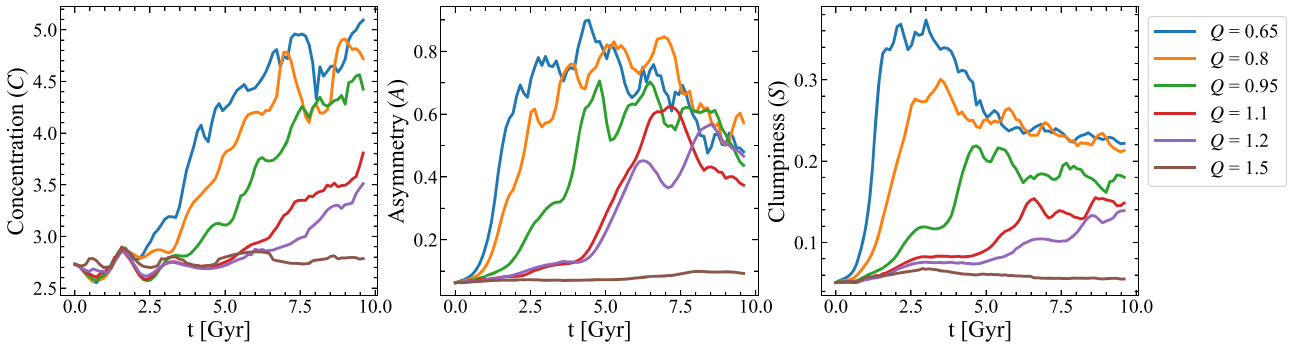

Figure 3. Time evolution of the CAS parameters from the simulation with $N = 5 \times 10^6$. The different colors in all panels represent the different values of Q, ranging from $Q = 0.65$ to $Q = 1.5$.

where Q was below 1 (Athanassoula 2003; Debattista et al. 2006; Worrakitpoonpon 2023). We have some important remarks for the latter regime that deserve attention. Our simulation of a $Q = 0.95$ disk demonstrates that first, the disk is populated by long-lasting clumps that persist until the end. Furthermore, the overall symmetry is strongly broken compared with the $Q = 1.1$ counterpart. These anomalies are attributed to the initial local instability. About the evolution pattern of the $Q = 0.65$ disk, there was a conjecture for a disk of comparable Q to be the progenitor of lenticular (or S0) galaxies, which do not host a bar and spiral arms (Saha & Cortesi 2018). This hypothesis is partly plausible for us as our simulations suggest that the S0 galaxy candidate can also emerge from $Q = 1.5$, i.e., when the disk is stable against all types of perturbations. The differentiation between the practically similar configurations originating from the locally stable and unstable disks needs a suitable indicator. These related properties are addressed in Section 4.2.

4.2. Evolution of the CAS Parameters

In continuity with the clumpy and asymmetric disks for $Q < 1$ observed in Section 4.1, we continue with a more systematic evaluation of these properties. Shown in Figure 3 are the time evolutions of CAS parameters for different Q. From the plots, we are able to classify the evolution schemes into three subfamilies: the $Q < 1$ disks, the $Q > 1$ disks that form a bar, and the disks that are bar-stable. Disks with $Q < 1$ develop highly concentrated, asymmetric, and clumpy features, as shown by the large increases in the three parameters. With a closer look, the clumpiness S increases most rapidly because of the local gravitational instabilities that reside in the initial state. It remains at its peak value for ∼2 Gyr before it decays sharply. Afterward, it continues to decay slowly until the end, but it is still higher than the other families. When Q is closer to 1, the S index develops more slowly and reaches a lower peak. This is because the disk is closer to the local stability threshold. The decline in S after the peak can be explained, in parallel with the evolution in Figure 2, by the reduced number of clumps with time. We recall that for $Q = 0.65$, the disk undergoes the formation of a clumpy multiarm pattern midway, in accordance with the time at which S peaks. At the end, a high level of clumpiness is still retained, although the clumpy spiral arms dissolve. Considering the concentration C and asymmetry A, they reach their peaks well after the S peak. This indicates that the developments of the C and A features are secondary processes that are induced by the clumpiness, which develops earlier. This order of increases is in accordance with the earlier speculation that anisotropically distributed clumps are the source of the asymmetry. Here, we confirm that the enhanced concentration is also a consequence. Considering the evolution of the A index, the values at the peak for $Q = 0.65$ and 0.8 are comparable, and they are significantly higher than the value for $Q = 0.95$. After the peaks, the A index for all three subcritical cases decreases. The rapid decay is explained by some clumps that fall to the disk center, resulting in the enhancement of C and the decline of S, accordingly. The C parameter, on the other hand, does not show any sign of decay with time until the end of the simulation, which indicates a continuous accumulation of density at the center by a merger with the clumps. In summary, the CAS evolution of this disk family is dominated by local instabilities that are marked by a rapid increase of S, followed by increases in C and A. We recall that the case when Q is far below 1 does not develop a barlike structure, while the cases starting with Q slightly below 1 can develop a bar. These differences cannot be distinguished by using the CAS parameters alone. A direct visual inspection of the disk configuration is required.

Disks that are bar-unstable and start with $Q > 1$ exhibit moderate increases in all CAS parameters, and the order of the increases differs from the order for $Q < 1$. The A parameter increases first due to the growth of two-armed modes that finally become the barred-spiral structure, and this established structure induces the growth of C and S. In this disk family, the linearly unstable two-armed modes play a central role, unlike in the situation of the previous disk family. Although the local gravitational instabilities are suppressed, C and S can nevertheless be enhanced by the bar and the two-armed modes, in line with the concentrated bar and spiral arms observed at the end in Figure 2, but they are not at the levels attained in a locally unstable disk. Close to the end of simulations, the A index decreases for $Q = 1.1$, which marks the onset of the decay of the bar modes, coherently with the decrease of A_2 in Figure 1. The case when $Q = 1.2$ does not yet exhibit a decay because the bar is formed later. In the bar-stable family, all parameters remain close to the initial values. This indicates that both local and bar-mode instabilities are effectively suppressed.

The variation in the CAS parameters can otherwise be plotted as a function of Q, as shown in Figure 4 at different times for $N = 5 \times 10^6$ and 10^6. The investigation of the case with a lower N has the purpose to examine how the results change when N is reduced since the clumps originate from the gravitationally unstable finite-N fluctuations, whose amplitudes scale with $1/\sqrt{N}$. In both cases, we observe that C and S tend to decrease as Q increases at 9.6 Gyr, as expected from a lower degree of local instabilities. With a closer look, the varying N

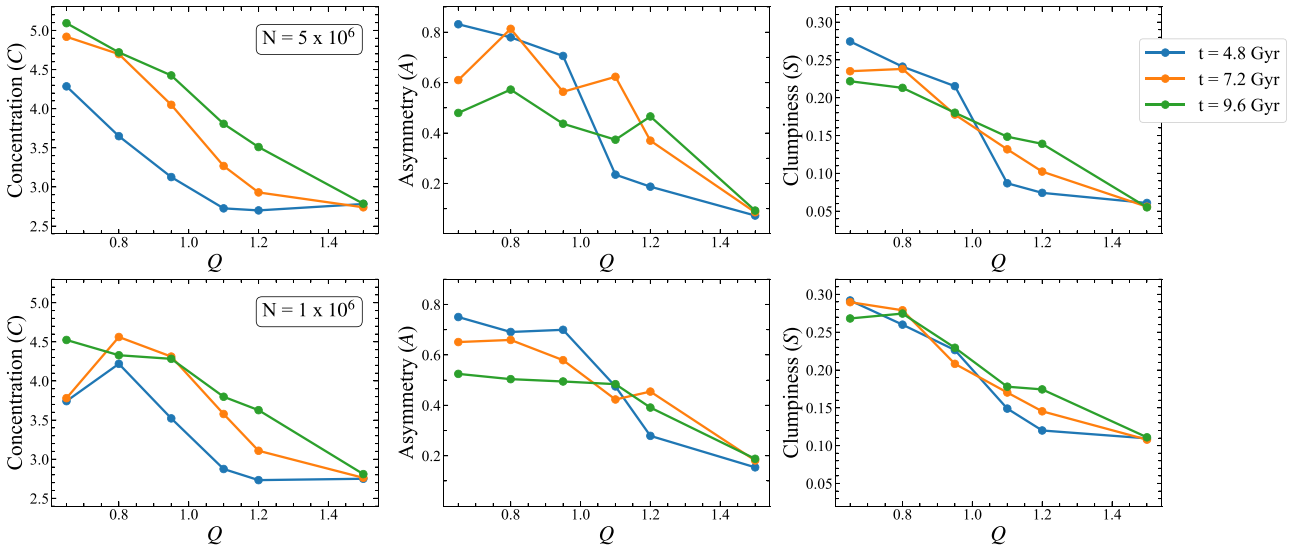

Figure 4. CAS parameters as a function of Q for $N = 5 \times 10^6$ (top panels) and $N = 1 \times 10^6$ (bottom panels). The solid blue, orange, and green lines indicate the snapshots at $t = 4.8$ Gyr, $t = 7.2$ Gyr, and $t = 9.6$ Gyr, respectively. The solid circles represent the values of Q we adopted in each simulation.

causes some notable differences in the evolutionary pattern and magnitude. The trivial consequence is that the S parameter for $N = 10^6$ is higher on average because the local instabilities are more pronounced. However, the decrease with Q is retained for both N. For the C parameter, it monotonically decreases with Q in all time snapshots for $N = 5 \times 10^6$. When N steps down to 10^6, the value for $Q = 0.65$ is significantly lower than the value for $Q = 0.8$ during 4.8–7.2 Gyr, but the monotonic decrease with Q is eventually achieved at 9.6 Gyr. This can be explained by the developed clumpy feature lasting longer when N is lower before it falls to the disk center. This speculation is supported by a slower decay of the S index from 4.8 to 9.6 Gyr than the decay rate for $N = 5 \times 10^6$. For the A parameter, the decrease with Q is more evident in the middle of the evolution because of the existing clumps and the forming barred-spiral structure, whereas there is no clear tendency of the variation with Q at the end. It turns out that using the A index as an indicator of the initial Q is best when the nonaxisymmetric features are at their peak. The variation in A with time and with Q for $N = 10^6$ is qualitatively similar to the $N = 5 \times 10^6$ counterpart: the decrease with Q is obvious at 4.8 Gyr, but the curve flattens in the range of $Q \leqslant 1.1$ in the end. In addition, the decay of S results in the decrease of A as some clumps are falling to the symmetric disk center and become part of it.

The inspection of the CAS parameters provides a new insight into the way in which the origin and evolution history of a disk of any morphology and structural detail can be specified. In the bar-forming regime with Q ranging from 0.8 to 1.2, disks starting with Q below and above 1 exhibit distinct evolutionary tracks of the CAS indices, and they lead to significantly different values. More specifically, barred galaxies that formed in $Q < 1$ disks can be identified by $C > 4.0$ and $S > 0.15$, referring to the case of $N = 5 \times 10^6$, and vice versa for bar-forming disks starting with $Q > 1$. Figure 3 suggests that the proposed C border value is applicable in the time frame of a galaxy age from 7 to 9.6 Gyr. The differentiation of the disk origin by this proposed S border value is applicable to a wider time frame of galaxy age: The value of $S = 0.15$ can distinguish the initial kinematical conditions of disk galaxies with ages from 5 to 9.6 Gyr. On the other hand, the A value can be useful when the asymmetric feature peaks. The clumpy barred-spiral disk can produce an A that is significantly greater than 0.6, and it saturates on this level for more than 4 Gyr. This is significantly greater than the asymmetry caused solely by the barred-spiral pattern, which can attain a value of around 0.6 for a short period of ∼0.5 Gyr at most before it starts to decay. The A parameter can therefore be used in the following way. An observed value of A greater than 0.6 can be evidence of a locally unstable initial disk. Otherwise, the establishment of barred-spiral galaxies without local instabilities cannot yield an A value greater than 0.6 in most of their lifetime.

Considering unbarred cases, this configuration can be achieved when Q is either far above or far below 1. Both cases yield a lenticular-like morphology at the end, but the measured CAS parameters are at remarkably different levels. The values of $C > 4.5$, $A > 0.4$, and $S > 0.2$ can indicate a cold progenitor of a lenticular disk, which undergoes violent evolution to form clumpy short-lived spiral arms. Orbiting clumps that remain are another piece of evidence of a cold origin. In contrast, those with modest CAS magnitudes undergo a smoother evolution without perturbative structures because all local and global nonaxisymmetric modes are suppressed. The C, A, and S values can be as low as 2.7, 0.1, and 0.05, respectively.

In observations, the concentration index increases with the increasing bulge-to-total ratio for the local galaxies (Conselice 2003). The early-type disk and elliptical galaxies, whose bulge is already well established, showed a concentration index of $C > 4.0$. Although this criterion is consistent with the simulated barred galaxies with $Q < 1$ in our simulations, the concentration index alone cannot be efficiently used to indicate a bar structure. The asymmetry index is frequently used to identify a merging system in both observations and simulations. Lotz et al. (2010a) used simulations to show that the asymmetry index could reach $A > 0.4$ at the stage of a final merger. It has later been used as the criterion for a merging system in observations (Kartaltepe et al. 2023). Considering our numerical results, a high level of the A index like this can be achieved and maintained for a long period in cases with $Q < 1$, whereas this level can be attained only for moments during the peak of the bar modes when $Q > 1$. Our important finding is that this high level of asymmetry can be attained

spontaneously in locally unstable disks. In the case of an isolated galaxy, the clumpy object can also show a high asymmetry index, as it is strongly correlated with the clumpiness (Conselice 2003). This correlation is also seen in our simulations (Figure 3). Early-type spiral and elliptical galaxies showed very low asymmetry ($A < 0.1$) and clumpiness ($S < 0.1$), while late-type spiral or starburst galaxies with a high star formation rate show higher values. The enhanced star formation in galaxies that exhibit a higher clumpiness index is actually understandable because the formation of the clumps also promotes the local star formation. This observed correlation emphasizes the possibility that a locally unstable disk is a progenitor of a clumpy spiral galaxy.

In summary, we find that the CAS parameters can be used for something in addition to their correlation with some current physical properties of galaxies, such as the bulge-to-total ratio and the star formation rate. The CAS magnitudes of an established disk galaxy of any morphology can determine its origin and evolution history reasonably well. Although our numerical model consists of purely self-gravitating particles, whereas a real galaxy consists of many components, the conclusion of the relation between the CAS values and the evolutionary history remains applicable. This is because the key factor leading to the difference, namely the local instability, is overseen by the gravity, and the gravity is the governing force of all components. In addition, it was documented that observed disk galaxies with an estimated Q lower than 1, in which local instabilities played a central role, tended to be gas-poor (Renaud et al. 2021; Aditya 2023). This ascertains that gravitational dynamics, which is our focus here, dominates the gas dynamics for this $Q < 1$ regime. Another limitation is that our study considers the evolution of a disk in isolation. A galaxy with a merger history might yield an elevated A without local instabilities, which might not conform with our conclusion.

4.3. Radial Heating with and without Clumps

It has been shown that the evolving nonaxisymmetric forces from the bar and the spiral arms could radially heat the disk environment, the so-called radial heating (Jenkins & Binney 1990; Minchev & Quillen 2006). Shown in Figure 5 is the radial velocity dispersion profile for $Q = 0.8$ and 1.1 at different times covering the process of the bar formation and its subsequent evolution. In both cases, we capture the radial heating as the profile raises with time, but the procedures are different in detail. For $Q = 1.1$, the entire profile heats up smoothly by global bisymmetric forces. In contrast, bumps in the profile of the $Q = 0.8$ case during the heating are spotted, most notably, at 3.84 Gyr. The bumps are lower but still observable at 6.72 Gyr, before the profile is smoothed out at 9.60 Gyr. We note that the final profile is flatter than the $Q = 1.1$ profile at the same time. These differences are attributed to the additional local heating by clumps, which is absent when $Q > 1$, in which case, the disk is heated by global bisymmetric forces without a local effect. The bumps in the profile during the radial heating and the flatness of the profile at the end can be indicative of a kinematically cold disk origin, in addition to the elevated CAS values that we addressed in the previous section.

The concept of radial heating by clumps shares similarities with the framework of heating by a giant molecular cloud (GMC) proposed by, for instance, Hänninen & Flynn (2002), Aumer et al. (2016), and Fujimoto et al. (2023). The major difference, however, is that these studies constructed the GMC in the context of a locally stable disk, i.e., $Q \geqslant 1$, while we inspect a locally unstable disk that spontaneously forms clumps. However, we do not rule out that this hypothesis is relevant as in reality, the disk kinematical map is not smooth and perfectly axisymmetric, as imposed in the initial conditions for our simulations. The GMC can potentially be formed in a location where the local Q is below 1, although the disk has $Q \geqslant 1$ on average.

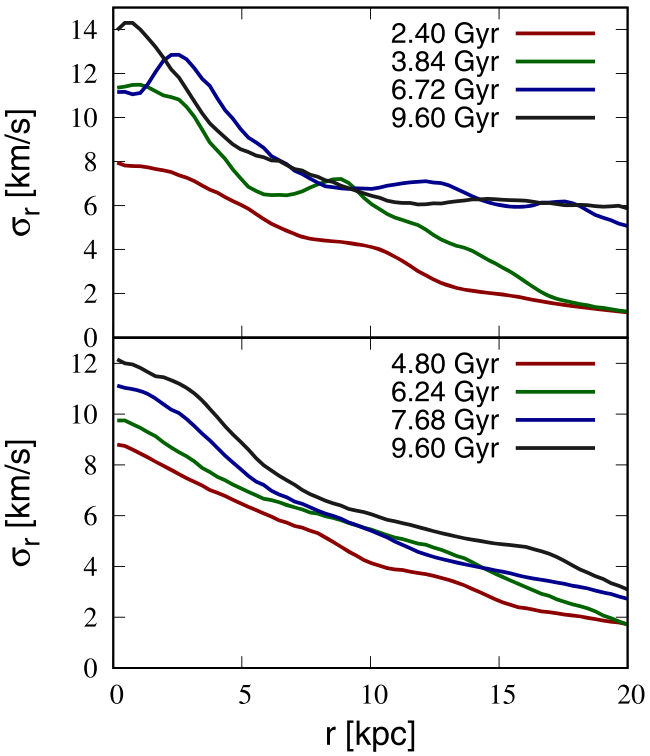

Figure 5. Radial velocity dispersion profiles at different times for $Q = 0.8$ (top panel) and 1.1 (bottom panel).

4.4. Lopsided Bar and Spiral Arms in Subcritical Q Disks

In continuity with the assumption of an apparently lopsided bar for the case where $Q = 0.95$ in Section 4.1, here we carry out a more systematic inspection of this appearance. It is common practice to probe the lopsidedness by A_1, and we inspect its evolution in time along with A_2. Shown in Figure 6 are the time evolutions of A_1 and A_2 for various Q. In all cases, the $m = 2$ modes are growing faster, and they lead to a barred structure when these modes peak. Afterward, the $m = 1$ modes are growing, whereas the $m = 2$ counterparts are decaying for cases with $Q = 0.8$ and 0.95, and the $m = 1$ modes become dominant at the end. The development of the $m = 1$ modes relative to the growth of A_2 for $Q = 0.95$ is slower than in the $Q = 0.8$ case because the local effect is weaker. The emerging lopsidedness as speculated by the dominance of A_1 is validated by Figure 7, which illustrates a lopsided barred-spiral disk around the time of the A_1 peak for $Q = 0.95$. The evolution schemes of A_1 and A_2 confirm our hypothesis in Section 3.1 that anisotropically distributed clumps cause the breaking of the bisymmetry. On the other hand, the $m = 1$ modes are not much amplified after the growth of the $m = 2$ modes when

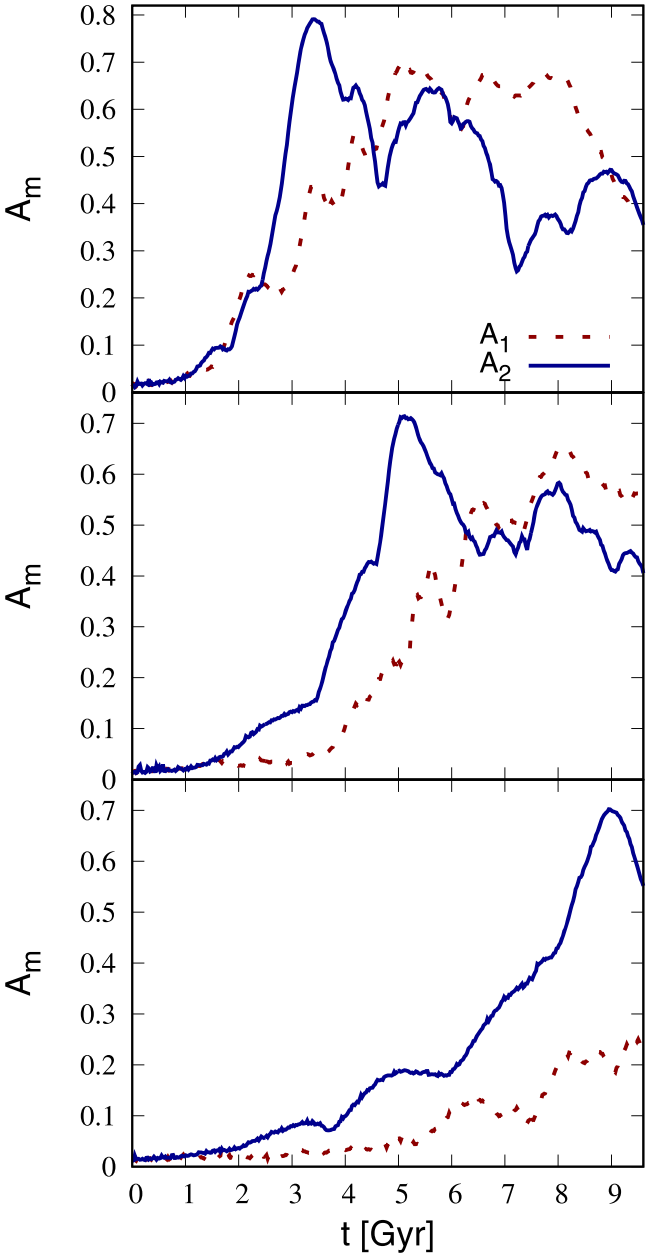

Figure 6. Time evolution of A_1 (dotted line) and A_2 (solid line) for $Q = 0.8$ (top panel), 0.95 (middle panel), and 1.1 (bottom panel).

$Q = 1.1$, and the latter modes remain the dominant modes until the end. This is because of the lack of local instabilities.

That the lopsided bar can potentially be established in a subcritical Q regime is an alternative explanation because previous studies often related the origin of the lopsided feature to the imposed macroscopic asymmetry of the initial state. For instance, the numerical results of Levine & Sparke (1998) and Łokas (2021) demonstrated that a disk that was initially off-centered from the halo origin could produce a lopsided bar. Other studies attributed the formation of a lopsided bar to tidal interactions (Yozin & Bekki 2014; Łokas 2022; Varela-Lavin et al. 2023). There were hypotheses that other astrophysical processes such as gas accretion (Bournaud et al. 2005; Dupuy et al. 2019) and stellar feedback (Manuwal et al. 2022) could generate the lopsidedness. Our important finding is that the established bisymmetry can spontaneously be broken and the

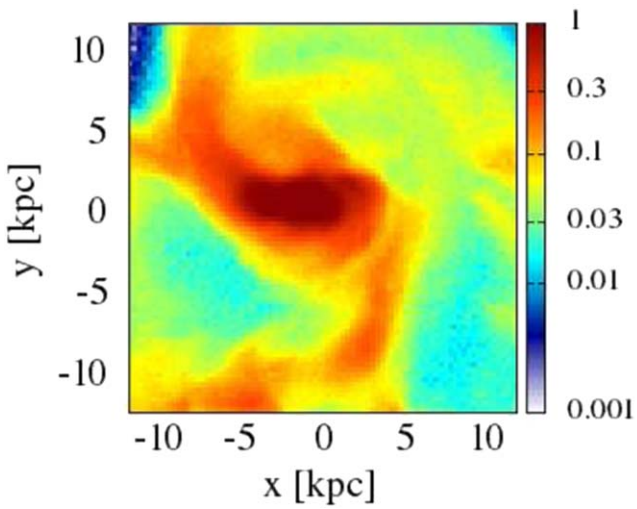

Figure 7. Surface density map of the disk center for $Q = 0.95$ at 6.96 Gyr.

disk becomes lopsided even when the initial disk is constructed from a circularly symmetric profile if the gravitationally unstable fluctuations are taken into account. In our framework, an initial asymmetry and external forces are not required.

5. Conclusion

We examine the evolution of disk galaxies in simulations for various initial Q values covering those that are below the Toomre stability threshold and those above it. The scope is not limited to the evolution of bisymmetric features alone, but we also investigate the development of the concentration, asymmetry, and clumpiness (CAS) properties in this range of Q. The CAS parameters are widely adopted to distinguish galaxies in observations, and we apply these parameters to our numerical results.

We find that CAS indices can be used when they are considered along with other conventional plots, such as the bar parameter or the density map, as they are able to identify the kinematical condition of the initial disk and the evolution history. For instance, the measured CAS values of cases that form a bar, which covers the initial $Q \in [0.8, 1.2]$, are able to distinguish them into two subgroups. A disk starting with $Q < 1$ develops a bar and clumps in parallel, yielding high CAS indices at the end, while the $Q > 1$ counterpart only develops a bar with a two-armed spiral pattern. In the latter group, the CAS values are significantly lower. For unbarred cases, which are candidates for a lenticular galaxy, this morphology can be obtained from an initial disk with Q either far below or far above 1. The distinction of unbarred disks achieved from these initial states at the two extremities can also be made using the CAS indices. The former case yields considerably higher CAS values than in the latter case. High CAS values in far subcritical Q disks also reflect a clumpy and asymmetric appearance, which is easy to determine visually.

In addition, the presence of long-lived clumps surrounding the barred-spiral structure can lead to remarkable outcomes. The first consequence is the distinct feature of the radial velocity dispersion profile caused by the local radial heating by clumps. It gives rise to bumps in the profile while the heating is progressing and to a flatter profile at the end than that without local heating. Second, the interactions between clumps and bisymmetric components are able to deform the bar to a

lopsided configuration. This is an alternative explanation of the formation of the lopsided bar apart from other scenarios, which require an initial seed of an asymmetry or external forces.

Acknowledgments

This research has received funding support from the NSRF via the Program Management Unit for Human Resources & Institutional Development, Research and Innovation (grant No. B16F640076). T.C. is supported by Naresuan University (NU) and by the National Science, Research and Innovation Fund (NSRF) grant No. R2566B091. T.W. has funding support from (i) Suranaree University of Technology (SUT), (ii) Thailand Science Research and Innovation (TSRI), and (iii) National Science, Research and Innovation Fund (NSRF, grant No. 179349). S.Y. is supported by Mahidol University (Fundamental Fund: fiscal year 2023 by National Science Research and Innovation Fund (NSRF)) and by the office of the Ministry of Higher Education, Science, Research and Innovation through a research grant for new scholars (RGNS63-175). Numerical simulations are facilitated by the HPC resources of the Chalawan cluster of the National Astronomical Research Institute of Thailand.

ORCID iDs

T. Chantavat https://orcid.org/0000-0002-0259-1591
S. Yuma https://orcid.org/0000-0002-0269-0135
T. Worrakitpoonpon https://orcid.org/0000-0002-0384-305X

References

Aditya, K. 2023, MNRAS, 522, 2543
Athanassoula, E. 2003, MNRAS, 341, 1179
Athanassoula, E. 2008, MNRAS, 390, L69
Athanassoula, E., Lambert, J. C., & Dehnen, W. 2005, MNRAS, 363, 496
Athanassoula, E., & Misiriotis, A. 2002, MNRAS, 330, 35
Athanassoula, E., & Sellwood, J. A. 1986, MNRAS, 221, 213
Aumer, M., Binney, J., & Schönrich, R. 2016, MNRAS, 462, 1697
Bauer, J. S., & Widrow, L. M. 2019, MNRAS, 486, 523
Bekki, K. 2023, MNRAS, 523, 5823
Bershady, M. A., Jangren, A., & Conselice, C. J. 2000, AJ, 119, 2645
Bournaud, F., Combes, F., Jog, C. J., & Puerari, I. 2005, A&A, 438, 507
Chiba, R., & Kataria, S. K. 2024, MNRAS, 528, 4115
Collier, A., Shlosman, I., & Heller, C. 2019, MNRAS, 488, 5788
Conselice, C. J. 2003, ApJS, 147, 1
Conselice, C. J. 2006, ApJ, 638, 686
Conselice, C. J. 2014, ARA&A, 52, 291
Conselice, C. J., Bershady, M. A., & Jangren, A. 2000, ApJ, 529, 886
Contopoulos, G., & Papayannopoulos, T. 1980, A&A, 92, 33
Curir, A., Mazzei, P., & Murante, G. 2006, A&A, 447, 453
De Rijcke, S., Fouvry, J.-B., & Pichon, C. 2019, MNRAS, 484, 3198
de Vaucouleurs, G. 1948, AnAp, 11, 247
Debattista, V. P., Mayer, L., Carollo, C. M., et al. 2006, ApJ, 645, 209
Domínguez Sánchez, H., Margalef, B., Bernardi, M., & Huertas-Company, M. 2022, MNRAS, 509, 4024
D'Onghia, E., Vogelsberger, M., & Hernquist, L. 2013, ApJ, 766, 34
Dupuy, J. L., Heitsch, F., & Cecil, G. 2019, MNRAS, 486, 2020
Efstathiou, G., Lake, G., & Negroponte, J. 1982, MNRAS, 199, 1069
Evans, N. W., & Read, J. C. A. 1998, MNRAS, 300, 106
Fischer, J. L., Domínguez Sánchez, H., & Bernardi, M. 2019, MNRAS, 483, 2057
Fujii, M. S., Bédorf, J., Baba, J., & Portegies Zwart, S. 2018, MNRAS, 477, 1451
Fujimoto, Y., Inutsuka, S.-i., & Baba, J. 2023, MNRAS, 523, 3049
Ghosh, S., & Jog, C. J. 2018, A&A, 617, A47
Goldreich, P., & Lynden-Bell, D. 1965, MNRAS, 130, 125
Hänninen, J., & Flynn, C. 2002, MNRAS, 337, 731
Hernquist, L. 1993, ApJS, 86, 389
Hohl, F. 1971, ApJ, 168, 343
Hozumi, S. 2022, MNRAS, 510, 4394
Hubble, E. P. 1926, ApJ, 64, 321
Jalali, M. A., & Hunter, C. 2005, ApJ, 630, 804
Jang, D., & Kim, W.-T. 2023, ApJ, 942, 106
Jenkins, A., & Binney, J. 1990, MNRAS, 245, 305
Joshi, R., & Widrow, L. M. 2024, MNRAS, 527, 7781
Julian, W. H., & Toomre, A. 1966, ApJ, 146, 810
Kalnajs, A. J. 1971, ApJ, 166, 275
Kartaltepe, J. S., Rose, C., Vanderhoof, B. N., et al. 2023, ApJL, 946, L15
Kataria, S. K., & Das, M. 2018, MNRAS, 475, 1653
Kataria, S. K., & Das, M. 2019, ApJ, 886, 43
Kataria, S. K., Das, M., & Barway, S. 2020, A&A, 640, A14
Kataria, S. K., & Shen, J. 2022, ApJ, 940, 175
Levine, S. E., & Sparke, L. S. 1998, ApJL, 496, L13
Li, X., Shlosman, I., Heller, C., & Pfenniger, D. 2023, MNRAS, 526, 1972
Lin, C. C., & Shu, F. H. 1964, ApJ, 140, 646
Łokas, E. L. 2021, A&A, 655, A97
Łokas, E. L. 2022, A&A, 662, A53
Long, S., Shlosman, I., & Heller, C. 2014, ApJL, 783, L18
Lotz, J. M., Jonsson, P., Cox, T. J., & Primack, J. R. 2008, MNRAS, 391, 1137
Lotz, J. M., Jonsson, P., Cox, T. J., & Primack, J. R. 2010a, MNRAS, 404, 575
Lotz, J. M., Jonsson, P., Cox, T. J., & Primack, J. R. 2010b, MNRAS, 404, 590
Manuwal, A., Ludlow, A. D., Stevens, A. R. H., Wright, R. J., & Robotham, A. S. G. 2022, MNRAS, 510, 3408
Michikoshi, S., & Kokubo, E. 2020, ApJ, 897, 65
Minchev, I., & Quillen, A. C. 2006, MNRAS, 368, 623
Ono, Y., Harikane, Y., Ouchi, M., et al. 2023, ApJ, 951, 72
Ostriker, J. P., & Peebles, P. J. E. 1973, ApJ, 186, 467
Papaderos, P., Östlin, G., & Breda, I. 2023, A&A, 673, A30
Renaud, F., Romeo, A. B., & Agertz, O. 2021, MNRAS, 508, 352
Romeo, A. B., Agertz, O., & Renaud, F. 2023, MNRAS, 518, 1002
Saha, K., & Cortesi, A. 2018, ApJL, 862, L12
Saha, K., & Elmegreen, B. 2018, ApJ, 858, 24
Saha, K., & Naab, T. 2013, MNRAS, 434, 1287
Sellwood, J. A. 1980, A&A, 89, 296
Sellwood, J. A. 2016, ApJ, 819, 92
Sellwood, J. A. 2021, MNRAS, 506, 3018
Sellwood, J. A., & Evans, N. W. 2001, ApJ, 546, 176
Sérsic, J. L. 1963, BAAA, 6, 41
Shen, J., & Sellwood, J. A. 2004, ApJ, 604, 614
Sheth, K., Elmegreen, D. M., Elmegreen, B. G., et al. 2008, ApJ, 675, 1141
Springel, V. 2005, MNRAS, 364, 1105
Springel, V., Yoshida, N., & White, S. D. M. 2001, NewA, 6, 79
Takeuchi, T. M., Ohta, K., Yuma, S., & Yabe, K. 2015, ApJ, 801, 2
Toomre, A. 1964, ApJ, 139, 1217
Toomre, A. 1981, in Structure and Evolution of Normal Galaxies, ed. S. M. Fall & D. Lynden-Bell (Cambridge: Cambridge Univ. Press), 111
Varela-Lavin, S., Gómez, F. A., Tissera, P. B., et al. 2023, MNRAS, 523, 5853
Vauterin, P., & Dejonghe, H. 1996, A&A, 313, 465
Worrakitpoonpon, T. 2023, ApJ, 958, 128
Yozin, C., & Bekki, K. 2014, MNRAS, 439, 1948
Yuma, S., Ohta, K., & Yabe, K. 2012, ApJ, 761, 19
Yuma, S., Ohta, K., Yabe, K., Kajisawa, M., & Ichikawa, T. 2011, ApJ, 736, 92
Zakharova, D., Sotnikova, N. Y., Smirnov, A. A., & Savchenko, S. S. 2023, MNRAS, 525, 2069